Editors' Suggestion

Flow structure and unsteadiness in a highly confined shock-wave–boundary-layer interaction

Jonathan Poggie* and Kevin M. Porter†
School of Aeronautics and Astronautics, Purdue University, West Lafayette, Indiana 47907, USA

(Received 6 October 2018; published 8 February 2019)

Numerical simulations were carried out to examine a 24° compression ramp interaction in which the confinement effect of sidewalls was very strong. The ratio of turbulent boundary-layer thickness to domain width at the start of the interaction was $\delta/w = 0.12$. Inflow conditions of $M_\infty = 2.25$ and $\mathrm{Re}_{\theta i} = 1800$ were chosen to match previous simulations. Comparing to the limited data available from similar computations, the centerline separation length scale L_s/δ was seen to vary with the flow confinement parameter δ/w, as previously recognized in reflected shock interactions. Significant differences in flow structure were observed between these computations with confining sidewalls and previous computations with periodic boundary conditions at the lateral boundaries of the domain. The most intense turbulent fluctuations occurred in the corners of the domain. Symmetric and antisymmetric motions of the separation region were identified in the instantaneous flow using conditional averages and spatial correlations. The presence of the sidewalls was found to influence both the mean and unsteady flow. Accurately capturing the sidewall flows is judged to be essential in realistic modeling of confined flows.

DOI: 10.1103/PhysRevFluids.4.024602

I. INTRODUCTION

The inherent three dimensionality and unsteadiness of separated shock-wave–boundary-layer interactions were identified in some of the earliest studies of the phenomenon [1,2]. Much research, however, has emphasized flows that are approximately two dimensional in the mean. This simplification has led to somewhat distorted perceptions of these interactions. For example, Green (see [3], p. 260) considered it remarkable that "a geometrically two-dimensional experimental arrangement can produce a highly three-dimensional flow."

A nominally two-dimensional geometry can become even more three dimensional when confined by sidewalls. The influence of the corner flow is significant for these cases. In applications, sidewall effects are particularly important, as in inlets and wind tunnels. Recent improvements in both experimental and computational techniques have allowed more detailed study of such flow three dimensionality [4–8].

Reda and Murphy [9,10] carried out early experimental studies on the effects of sidewalls on reflected shock-wave–boundary-layer interactions, showing the highly nonuniform surface oil flow pattern that occurs under certain conditions [9]. (A good photograph of this type of pattern is given in Fig. 16 of [3].) More recently, Babinsky and co-workers [11,12] have carried out extensive experimental investigations of the influence of sidewalls and identified the parameter δ/w, where

*jpoggie@purdue.edu
†Present address: Lockheed-Martin Corporation, Palmdale, CA 93599, USA; porter28@purdue.edu

δ is the boundary-layer thickness and w is the duct width, as key in controlling boundary-layer blockage and flow three dimensionality.

According to Babinsky *et al.* [12], a relationship exists between the aspect ratio δ/w and the streamwise separation length scale L_s at the interaction centerline. (Here L_s is the streamwise distance between points where the streamwise shear stress crosses zero.) For $\delta/w \ll 1$ (a wide duct), a quasi-two-dimensional flow is expected. For moderate values of this aspect ratio, increased L_s is expected, with increased mean-flow three dimensionality. For larger values of δ/w (a narrow duct), L_s is expected to decrease again and a strong interaction between the corner flows should occur. These flow changes have been observed in Reynolds-averaged Navier-Stokes simulations of reflected shock interactions [13,14]. According to these simulations, the peak streamwise extent of separation occurs near $\delta/w = 0.06$. The approach to the limit $\delta/w \ll 1$ is slow: Significant differences from a two-dimensional simulation ($\delta/w = 0$) occur even for $\delta/w = 0.015$, a case with very thin boundary layers.

These three-dimensional effects have been explored in high-fidelity simulations. Garnier [15] carried out stimulated detached eddy simulations of a Mach 2.3 experiment with a 9.5° shock generator, accounting for the full wind tunnel span. The author reported that the presence of the lateral walls strengthened the shock interaction and that the most intense pressure fluctuations occurred in the corner flow regions.

In other recent studies, Funderburk and Narayanaswamy [16] carried out experiments investigating the unsteadiness of a 12° compression ramp interaction at Mach 2.5, with a high degree of flow confinement ($\delta/w = 0.14$) but a small streamwise separation scale ($L_s/\delta = 0.8$). They found that the corner and centerline regions differed in their unsteady features and response to perturbations. Morgan *et al.* [17] carried out large-eddy simulations of a choked duct flow at Mach 1.6 and observed a strong effect of the sidewall interaction on the shock train dynamics. Wang *et al.* [18] studied an oblique shock-wave–boundary-layer interaction at Mach 2.7. The analysis focused on the effect of the duct aspect ratio on the mean flow and on distortion of the flow structure from two-dimensional cases.

Bisek [19] carried out simulations of a Mach 2.25, 24° compression ramp interaction with an aspect ratio of $\delta/w = 0.06$. Comparison of a half-span calculation (one viscous wall and a centerline symmetry boundary condition) to a full-span calculation (two viscous walls) showed important differences. In particular, the half-span calculations showed a delay of separation relative to the full-span calculations. Analysis of the instantaneous wall pressure in the full-span calculations showed intermittent patterns of corner separation: The instantaneous pattern could be either roughly symmetric or antisymmetric at large scale.

Here we extend the previous computational work on corner flow influence in compression ramp interactions. Inflow conditions of $M_\infty = 2.25$ and $\mathrm{Re}_{\theta i} = 1800$ were chosen to approximately match previous simulations [19]. With the caveat that only a few of these costly simulations are available for comparison, we aim to explore the effect of the domain width parameter δ/w on the flow structure of a 24° compression ramp interaction. The present flow has very high three dimensionality, with an aspect ratio of $\delta/w = 0.12$. The configuration is close to the limit of flow choking.

II. METHODS

The physical model employed in this project was the ideal-gas, compressible-flow Navier-Stokes equations. The usual constitutive equations were employed: Newtonian viscous friction and the Fourier heat conduction law. The transport equations were evaluated from standard correlations [20], with an assumption of constant Prandtl number and specific heat.

The calculations were carried out using an in-house code (HOPS), which was implemented in modern FORTRAN [21]. Parallel calculations with domain decomposition were implemented using the MPI library. Outer loop threading with OpenMP for each subdomain extended parallel performance to higher core counts. Input and output were implemented using MPI-IO.

A. Numerical approach

Spatial discretization was carried out using compact difference methods [22–24]. Applying this approach in one-dimensional transformed coordinates, the finite-difference approximation to the first derivative ϕ_i' is evaluated by solving a tridiagonal system of the form

$$\alpha\phi'_{i-1} + \phi'_i + \alpha\phi'_{i+1} = a\frac{\phi_{i+1} - \phi_{i-1}}{2} + b\frac{\phi_{i+2} - \phi_{i-2}}{4}, \tag{1}$$

where α, a, and b are constants chosen to give a certain order of accuracy and set of spectral properties for the scheme. In the center of the domain, a sixth-order compact difference method was employed. Near boundaries the order of accuracy of the compact difference method was reduced: A fifth-order method was used for the point adjacent to the boundary and a fourth-order method was used at the boundary.

In regions away from shocks, stability was enforced using Padé-type nondispersive spatial filters [23,24]. The filter was applied to the solution vector, sequentially, in each of the three computational directions, following each subiteration in implicit time integration. The filtering approach replaces the computed value ϕ_i at a particular node with a filtered value $\overline{\phi}_i$,

$$\alpha_f\overline{\phi}_{i-1} + \overline{\phi}_i + \alpha_f\overline{\phi}_{i+1} = \sum_{n=0}^{N}\frac{a_n}{2}(\phi_{i+n} + \phi_{i-n}), \tag{2}$$

where the constants $\alpha_f, a_0, \ldots, a_N$ are chosen to give appropriate filter properties. An eighth-order filter was used in the center of the domain and the order of filter accuracy was reduced in steps of 2 as a boundary was approached, with no filtering at the boundary. The form of the filter function can be adjusted by varying the free parameter in the range $-1/2 < \alpha_f < 1/2$; here we used $\alpha_f = 0.40$ with the eighth-order filter and $\alpha_f = 0.49$ with the lower-order filters.

Shock capturing was implemented using a method based on the approach of Visbal and Gaitonde [25]. In the present work, shocks were identified using the pressure-based shock sensor of Swanson and Turkel [26],

$$\phi = \frac{|p_{i+1} - 2p_i + p_{i-1}|}{(1-\omega)(|p_{i+1} - p_i| + |p_i - p_{i-1}|) + \omega(p_{i+1} + 2p_i + p_{i-1})}, \tag{3}$$

where the parameter lies in the range $0 < \omega \leqslant 1$. Here we take $\omega = 0.5$. For the present work, we considered a cell to contain a shock if the sensor exceeded the threshold $\phi > 2 \times 10^{-3}$ and the local Mach number was supersonic, $M > 1.05$.

Once the shock was identified, a buffer region of at least five cells was identified around the shock, and in these cells the Roe scheme [27] was used. Extrapolation to cell boundaries was carried out using a third-order upwind-biased scheme based on the monotone upstream schemes for conservation laws (MUSCL) formulation [28]. The present work used the continuous limiter of Anderson *et al.* [28],

$$s = \frac{2\Delta_+\Delta_- + \epsilon}{\Delta_+^2 + \Delta_-^2 + \epsilon}, \tag{4}$$

where $\Delta_+ = f_{i+1} - f_i$, $\Delta_+ = f_i - f_{i-1}$, f_i is a solution variable, and $\epsilon = 1 \times 10^{-12}$ is an arbitrary small value. The filter was not applied in the shock region and the order of the filter was increased away from the shock in the manner employed near boundaries. The compact difference formulation was interrupted by the shock region; second-order explicit differences were used within the shock region where needed.

Time integration was carried out using an approximately factored second-order scheme. The scheme is essentially the same as that employed by Visbal and Rizzetta [29], and full details are presented in that reference. The equations were solved in Δ form, using a subiteration scheme that drives the change in the solution vector to zero [21]. For the present work, three applications of the flow solver were carried out per time step. The implicit scheme used the scalar pentadiagonal

TABLE I. Flow conditions.

Parameter	Value
U_∞	588 m/s
M_∞	2.25
T_∞	170 K
T_w	323 K
p_∞	2.383×10^4 Pa
δ_0	6.096×10^{-4} m
ramp angle	24°
domain width w	$20\delta_0$
corner location x	$100\delta_0$

approach of Pulliam and Chaussee [30] and the implicit damping approach of Pulliam and Steger [31]. Implicit damping coefficients of $\epsilon_2^{(i)} = 0.2$ and $\epsilon_4^{(i)} = 0.1$ were used. Grid metrics were evaluated using the method of Thomas and Lombard [32].

B. Compression ramp flow

The flow conditions (Table I) were chosen to match those of certain previous computations of boundary layers and compression ramp interactions [19,21,33–37]. A comparison with experiment for the incoming turbulent boundary layer will be presented in Sec. III B.

The computational mesh is shown in Fig. 1. For clarity, only every 32nd point is shown. No-slip conditions were imposed at the bottom and sides of the domain. Grid clustering was employed near the three no-slip walls and near the corner of the ramp. At the front of the domain, the incoming boundary-layer profile was set to match a laminar-flow similarity solution for the selected flow conditions. Interpolation was used to produce smooth flow in the corners of the domain. Extrapolation was employed at the end and top of the domain to implement an outflow boundary condition. Grid stretching was employed in these outflow regions; this is visible at the top right of Fig. 1. To support this sponge layer and eliminate any wave reflections, the filter was changed to second order, with $\alpha_f = 0.40$, for the four cells nearest the boundary.

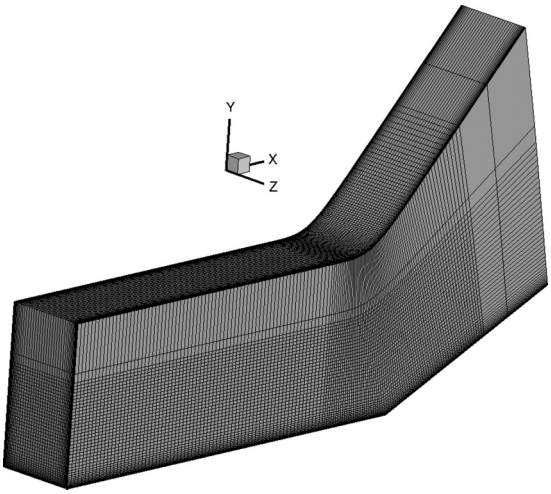

FIG. 1. Computational mesh of 4711 × 1421 × 1401 points; every 32nd point is shown for clarity.

The space and time resolution of the calculations conform to the recommendations of Georgiadis *et al.* [38] for resolved turbulent simulations. The grid consisted of 9.4×10^9 cells in a structured $4711 \times 1421 \times 1401$ mesh. The mesh spacing in the primary flow direction (ξ direction or i direction of the mesh) was $\Delta_\xi/\delta_0 = 3.48 \times 10^{-2}$. For the direction approximately normal to the floor of the domain (η direction or j direction), the mesh spacing ranged from $\Delta_\eta/\delta_0 = 2.25 \times 10^{-3}$ at the wall to $\Delta_\eta/\delta_0 = 3.48 \times 10^{-2}$ in the core flow. Similarly, for the transverse direction (ζ direction or k direction), the mesh spacing ranged from $\Delta_\zeta/\delta_0 = 2.24 \times 10^{-3}$ at the two walls to $\Delta_\zeta/\delta_0 = 2.35 \times 10^{-2}$ in the core flow.

The corresponding wall-normal resolution in inner units at the reference boundary-layer station at $x/\delta_0 = 80$ was $\Delta_\eta^+ = 0.51$ at the center of the floor boundary layer ($y/\delta_0 = 0$ and $z/\delta_0 = 10$). For corresponding stations near the centers of the sides ($y/\delta_0 = 8.6$ and $z/\delta_0 = 0, 20$), the wall-normal resolution was $\Delta_\zeta^+ = 0.51$. At the edge of the boundary layer, the nondimensional grid spacing was $\Delta_\xi^+ = 7.9$, $\Delta_\eta^+ = 7.9$, and $\Delta_\zeta^+ = 5.3$.

Transition to turbulent flow was promoted using an artificial body-force trip based on the approach of Mullenix *et al.* [39]. The trip was implemented at $x/\delta_0 = 2.50$ for all three sidewalls. In contrast to some of our previous work, here the trip was chosen to be essentially uniform along the boundary-layer span, although it was set to zero for a small region in the corners. For the region near $y/\delta_0 = 0$, the trip was imposed for $0.25 \leqslant z/\delta_0 \leqslant 19.75$, and for the region near $z/\delta_0 = 0$ and near $z/\delta_0 = 20.00$, the trip was imposed for $0.25 \leqslant y/\delta_0 \leqslant 24.00$.

The trip had the following form near the bottom ($y/\delta_0 = 0$) wall:

$$F(x, y, z) = \frac{A}{\pi x_r y_r} \exp\left[-\left(\frac{x - x_1}{x_r}\right)^2 - \left(\frac{y - y_1}{y_r}\right)^2\right] \Pi_{z_a, z_b}(z),$$
$$f_x = F(x, y, z)\cos\theta, \quad f_y = F(x, y, z)\sin\theta, \quad f_z = 0. \tag{5}$$

This body force was added to the momentum equation and its corresponding work was added to the total energy equation. The final term is the unit boxcar function, defined here as

$$\Pi_{a,b}(x) = \begin{cases} 0, & x < a \\ 1, & a \leqslant x \leqslant b \\ 0, & x > b. \end{cases} \tag{6}$$

Here the position of the center of the trip was $x_1/\delta_0 = 2.50$ and $y_1/\delta_0 = 0.00$, its scale was $x_r/\delta_0 = 0.17$ and $y_r/\delta_0 = 0.01$, and the position of the boxcar masking in the z direction was $z_a/\delta_0 = 0.25$ and $z_b/\delta_0 = 19.75$. For all the walls, the amplitude of the trip force was taken to be $A = 0.03$ and the angle was taken as $\theta = 179^\circ$.

The artificial body force had the following analogous form near the $z/\delta_0 = 0$ wall:

$$F(x, y, z) = \frac{A}{\pi x_r z_r} \exp\left[-\left(\frac{x - x_1}{x_r}\right)^2 - \left(\frac{z - z_1}{z_r}\right)^2\right] \Pi_{y_a, y_b}(y),$$
$$f_x = F(x, y, z)\cos\theta, \quad f_y = 0, \quad f_z = F(x, y, z)\sin\theta. \tag{7}$$

Here the position of the center of the trip was $x_1/\delta_0 = 2.5$ and $z_1/\delta_0 = 0.00$ and the length scale was $x_r/\delta_0 = 0.17$ and $z_r/\delta_0 = 0.01$. The position of the boxcar masking in the y direction was $y_a/\delta_0 = 0.25$ and $y_b/\delta_0 = 24.00$. The form of the trip at the $z/\delta_0 = 20.00$ wall was the same, except that the direction of the f_z force component was reversed, and the center of the trip was changed to $z_1/\delta_0 = 20.00$.

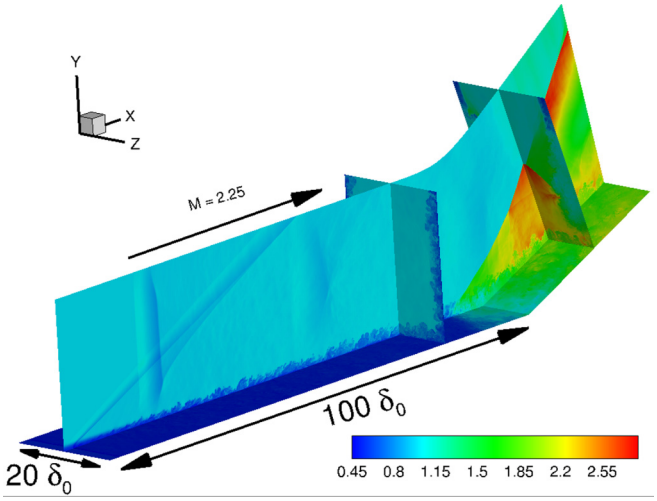

FIG. 2. Overview of the flow field, showing the instantaneous density field in several planes.

The main calculations were carried out on the IBM Blue Gene/Q machine Mira at Argonne Leadership Computing Facility. The computational mesh was divided into 65 536 subdomains in a $64 \times 32 \times 32$ configuration, with nine-point overlap, and with one MPI rank assigned to each subdomain. Eight OpenMP threads were assigned to each zone to exploit loop-level parallelism, for at total of 524 288 cores employed in the computation.

The nondimensional time step was $U_\infty \Delta t/\delta_0 = 5 \times 10^{-3}$, or $\Delta t^+ = 5.3 \times 10^{-2}$ based on the reference incoming boundary-layer station. The computations were run for 239 000 iterations, corresponding to a simulation time of $U_\infty t/\delta_0 = 1195.0$. The calculation was initially run for just over two flowthrough times ($U_\infty t/\delta_0 = 288.0$) to allow a statistically steady state to be established and then flow data were saved for statistical analysis for about 7.0 flowthrough times ($U_\infty t/\delta_0 = 907.0$). The data were saved every 200 iterations ($U_\infty \Delta t/\delta_0 = 1.0$).

Large-scale separation motion has been characterized by a Strouhal number $\mathrm{St} = f_s L_s/U_\infty$, where f_s is the location of the low-frequency peak in the premultiplied spectrum and L_s is a separation length scale [40,41]. A range of Strouhal numbers distinguish different shock-wave–boundary-layer interactions. Nevertheless, a figure of $\mathrm{St} = 0.03$ is often cited as a representative value. The duration of the present data set corresponds to about 5.3 cycles of motion at the $\mathrm{St} = 0.03$ scale. Thus, the present work focuses on midscale motions of the separation region. (See [42] for a discussion of typical flow modes observed in a separated shock-wave–boundary-layer interaction.)

III. RESULTS

We begin our discussion of the results by describing the overall structure of the flow field, emphasizing that this is a duct flow, not a canonical two-dimensional interaction. In order to document the inflow conditions for the separated region, we then present detailed results for the incoming turbulent boundary layer and compare them to other simulations and to experimental data. We explore the details of the region of flow separation next and finally we examine symmetry and antisymmetry in the instantaneous flow field.

A. Overall flow structure

An overview of the flow field is presented in Fig. 2, which shows the instantaneous density field in several planes. These planes include the floor of the computational domain (minimum y coordinate), the center plane ($z/\delta_0 = 10$), a plane representative of the developed incoming turbulent boundary

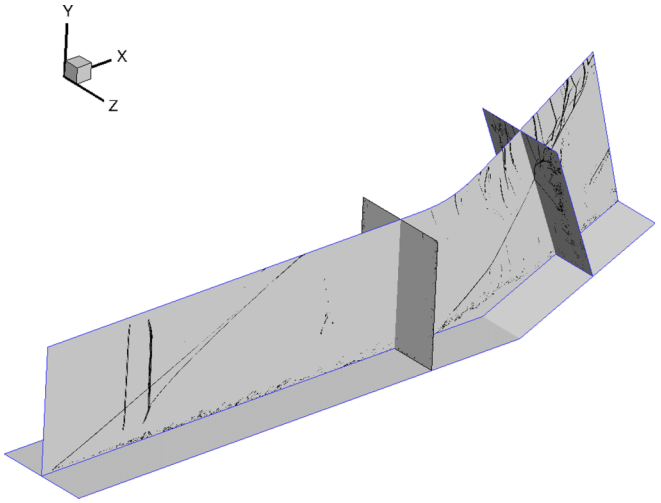

FIG. 3. Behavior of the shock sensor at a particular instant. Black indicates locations where the sensor is triggered.

layer ($x/\delta_0 = 80$), and a plane normal to the ramp ($x/\delta_0 \approx 111$). The inlet flow lies at the lower left in the figure ($x/\delta_0 = 0$). As indicated, the domain is $20\delta_0$ wide and the corner of the ramp lies at $x/\delta_0 = 100$. The laminar boundary imposed at the inlet is allowed to develop downstream until it reaches the body-force trip at $x/\delta_0 = 2.5$. Weak waves from the trip are evident in the center-plane density field. Waves from the sidewall trips intersect the center plane, as do wave reflections further downstream. A turbulent boundary layer is seen to develop on the three no-slip boundaries of the domain (irregular dark blue contour at $x/\delta_0 = 80$). A complex shock-wave–boundary-layer interaction occurs as the boundary layer encounters the strong pressure gradient introduced by flow turning at the ramp.

For reference, Fig. 3 shows the locations where the shock sensor (3) indicates the presence of a shock. Black denotes locations where the shock sensor is on; gray indicates regions where it is off. (The solution time here is not the same as in Fig. 2.) The sensor is triggered by shocks and by local regions with very strong pressure gradient.

During the computations, data were saved for six planes within the computational domain: the three no-slip walls, the $x/\delta_0 = 80$ plane, the ramp-normal plane ($x/\delta_0 \approx 111$), and the portion of the center plane ($z/\delta_0 = 10$) downstream of $x/\delta_0 = 80$. Results for the three planes in the interior of the domain are presented here.

Figure 4 shows the density field in the $x/\delta_0 = 80$ plane. The view is along the x axis, looking downstream. A sample of the instantaneous density field ρ/ρ_∞ is shown in Fig. 4(a). The grayscale contours were intentionally chosen to appear similar to planar laser visualization data [43]. The dark irregular region along the sides of the domain indicates the hot low-density turbulent fluid in the turbulent boundary layer along the three no-slip walls. The light central region represents the cold high-density core flow. Close inspection of the central portion of the domain reveals density fluctuations due to sound radiated from the boundary-layer turbulence. Since the acoustic field is confined on three sides by the no-slip walls, the reverberation effect is stronger than it would be in less confined flows. The corresponding mean density field is shown in Fig. 4(b). The smooth variation of the mean boundary layer around the edges of the domain is evident in these data, as are some persistent weak waves in the core flow.

Figure 5 shows the plane normal to the ramp, where $x/\delta_0 \approx 111$. The wave structure in this plane corresponds to a very narrow compression ramp interaction (central region in the z direction), with two fin interactions on the sides (λ-shock patterns). Slip lines are evident, originating at the

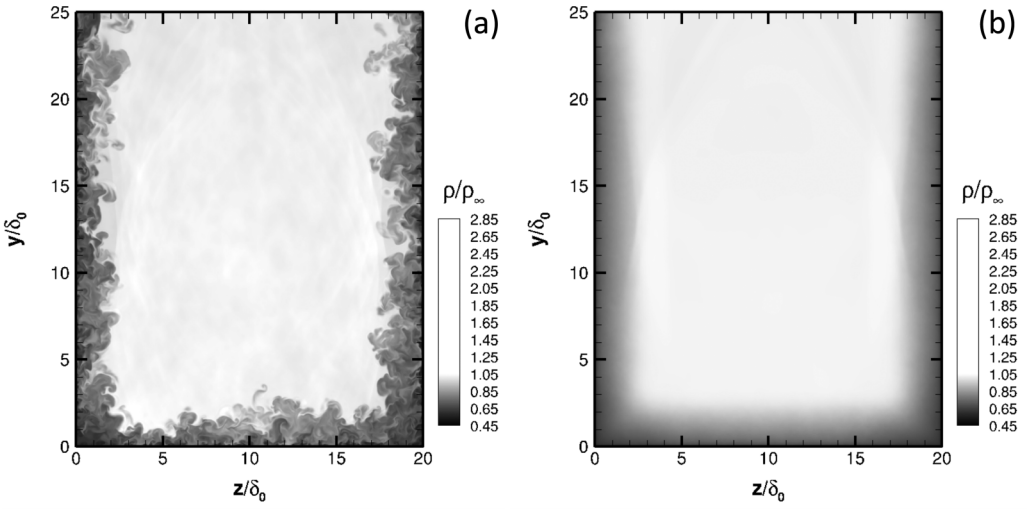

FIG. 4. Density field in the $x/\delta_0 = 80$ plane: (a) instantaneous and (b) mean.

triple points of the λ shocks. Movies of this region of the flow dramatically illustrate its intense unsteadiness, and some indication of this unsteadiness is apparent in the instantaneous density field of Fig. 5(a). The overall flow structure is similar in the mean density field [Fig. 5(b)], with significant smearing of the shocks due to their unsteadiness. Note also the displacement of the shock triple points in the instantaneous field relative to the mean field. Turbulence modeling of such an unsteady flow is expected to be extremely challenging.

Figure 6 shows the density field in the $z/\delta_0 = 10$ plane, a side view of the interaction region in the center plane. The instantaneous field is shown in Fig. 6(a) and the corresponding mean in Fig. 6(b). The floor turbulent boundary layer is apparent at the bottom of the field of view. It enters from the left and encounters the flow separation at $x/\delta_0 \approx 90$. Flow separation is associated with the

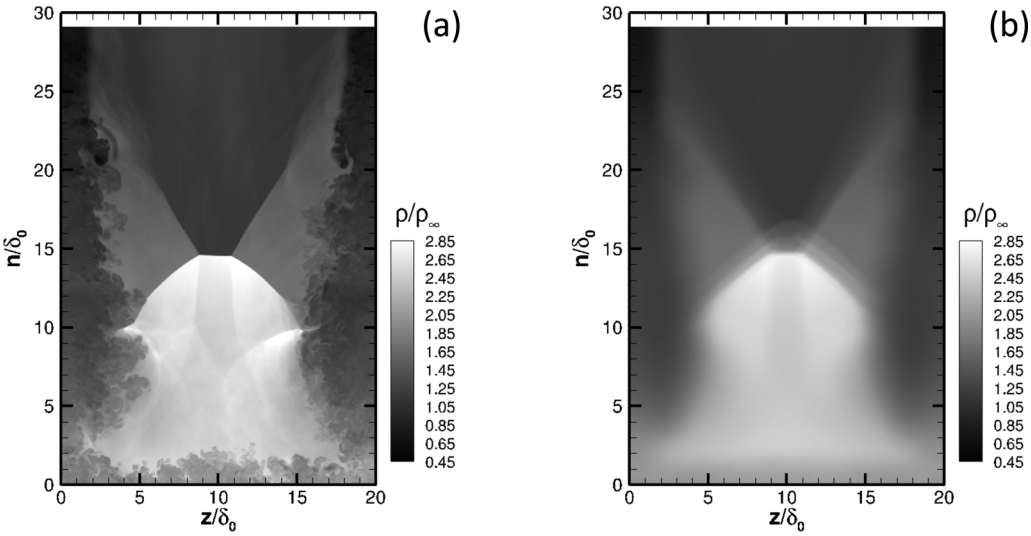

FIG. 5. Density field in the plane normal to ramp, $x/\delta_0 \approx 111$: (a) instantaneous and (b) mean. The coordinate n is the distance from the ramp surface.

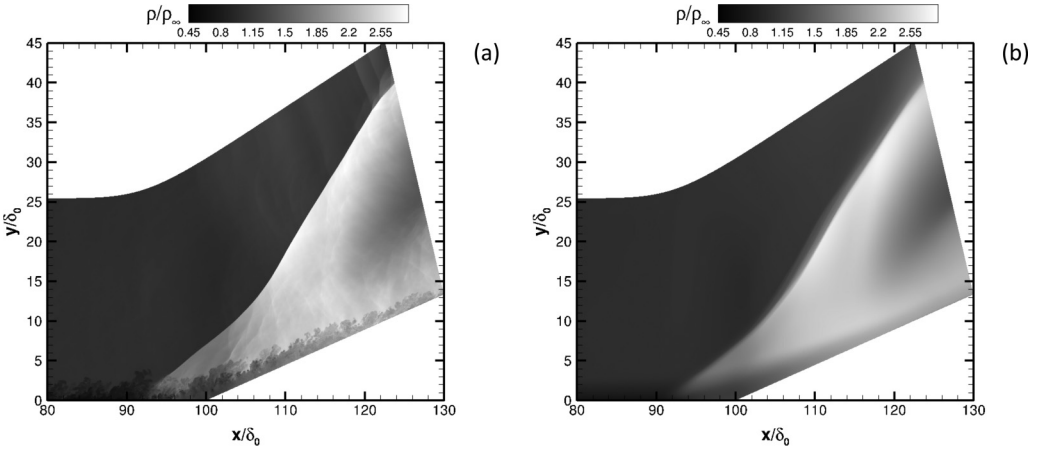

FIG. 6. Density field in the $z/\delta_0 = 10$ plane: (a) instantaneous and (b) mean.

classic λ-shock pattern of a compression ramp interaction. In the instantaneous flow, shocks are seen emanating from turbulent structures and the primary oblique shock is curved due to out-of-plane interaction with the sidewall flows. Various transient waves are also discernible in the instantaneous core flow. In the mean [Fig. 6(b)], many of these features are washed out. It is again worth noting the blurring of the shocks in the mean flow due to their unsteadiness.

B. Boundary-layer data

To document the inflow boundary conditions for the shock-wave–boundary-layer interaction, data were extracted for the floor boundary layer and the sidewall boundary layers for the streamwise station $x/\delta_0 = 80$ (see Fig. 4). The data labeled "floor" correspond to the station $x/\delta_0 = 80$ and $z/\delta_0 = 10$, with the wall normal in the y direction. The side profiles correspond to $x/\delta_0 = 80$ and $y/\delta_0 = 10$. For the left side, the wall is at $z/\delta_0 = 0$ with the wall normal in the z direction, and for the right side, the wall lies at $z/\delta_0 = 20$ and the wall normal lies in the $-z$ direction.

Some basic boundary-layer data are presented in Table II. Here the boundary-layer thickness parameters are referenced to the thickness δ_0 of the laminar boundary layer imposed at the inflow plane (see Table I). The boundary-layer thickness is seen to grow to $2.4\delta_0$ over the first $80\delta_0$ of the domain. The resulting momentum thickness Reynolds number is $\mathrm{Re}_\theta = \rho_\infty U_\infty \theta/\mu_\infty = 3000$ or $\mathrm{Re}_{\theta i} = \rho_\infty U_\infty \theta/\mu_w = 1800$. The skin friction coefficient is 2.4×10^{-3} and the friction Reynolds number is $\delta^+ = u_\tau \delta/\nu_w = 540$. The shape factor for the floor boundary layer is $H = \delta^*/\theta = 3.5$, consistent with experimental measurements at similar flow conditions [44,45]. (The corresponding incompressible shape factor, ignoring density variation, is about 1.4.)

TABLE II. Boundary-layer properties at $x/\delta_0 = 80$.

Parameter	Floor	Left	Right
δ/δ_0	2.36	2.27	2.28
δ^*/δ_0	0.67	0.74	0.74
θ/δ_0	0.19	0.17	0.17
Re_θ	3000	2600	2600
$\mathrm{Re}_{\theta i}$	1800	1600	1600
δ^+	540	510	510
C_f	2.36×10^{-3}	2.43×10^{-3}	2.46×10^{-3}

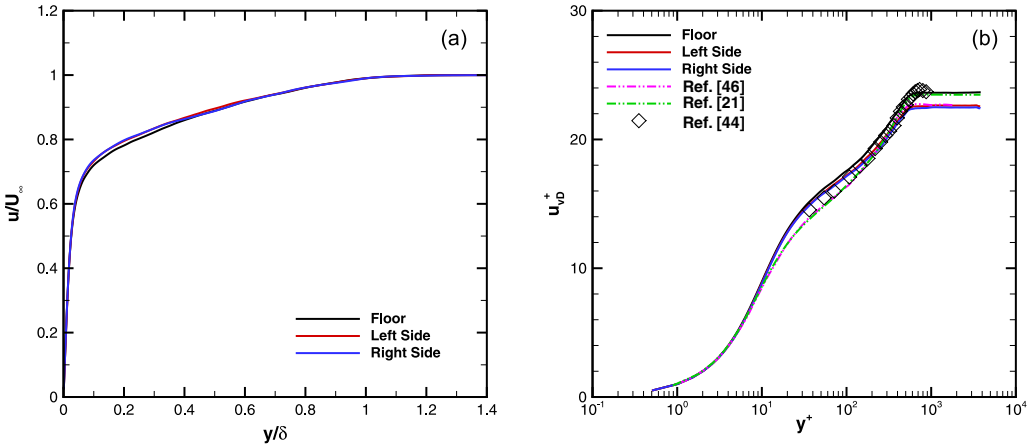

FIG. 7. Turbulent boundary-layer profiles on the floor ($x/\delta_0 = 80$ and $z/\delta_0 = 10$) and sides of the domain ($x/\delta_0 = 80$ and $y/\delta_0 = 10$) compared to DNS [21,46] and to experiment [44]: (a) outer coordinates and (b) van Driest transformed inner coordinates. The horizontal axis represents the wall-normal coordinate in each case.

Mean velocity profiles are presented in outer coordinates in Fig. 7(a) and in [47] transformed inner coordinates in Fig. 7(b). For these, and subsequent, boundary-layer plots, the coordinates have been rotated so that the coordinates (x, y, z) and velocity components (u, v, w) correspond to the streamwise, wall-normal, and spanwise directions for the local boundary layer. The boundary-layer data from the present computations were compared to those from the highly resolved boundary-layer simulations of Pirozzoli and Bernardini [46] ($M = 2.0$ and $\mathrm{Re}_{\theta i} = 1.5 \times 10^3$) and of Poggie *et al.* [21] ($M = 2.25$ and $\mathrm{Re}_{\theta i} = 2.0 \times 10^3$) and to the experimental data of Éléna and Lacharme [44] ($M = 2.3$ and $\mathrm{Re}_{\theta i} = 2.6 \times 10^3$).

Corresponding Reynolds stress profiles, using Morkovin [48] density scaling, are shown in Fig. 8. The present numerical results are compared to the direct numerical simulation (DNS) of Poggie *et al.* [21], the laser Doppler anemometry measurements of Éléna and Lacharme [44] ($M = 2.3$, $\mathrm{Re}_{\theta i} = 2600$), and the hotwire measurements of Alving [49] ($M = 0$, $\mathrm{Re}_\theta = 5000$). Where available, error bars corresponding to the statistical uncertainty reported for the experiments are included in the plots. The results are plotted in outer coordinates, and collapse of the data for the differing Reynolds numbers should be expected for the outer portion of the profiles (roughly, $y/\delta > 0.2$).

Data were also extracted for a boundary-layer station on the ramp (see Fig. 5) and compared to the incoming boundary layer. The coordinate system was rotated appropriately to boundary-layer coordinates. The results are shown in Fig. 9 in both outer coordinates and van Driest transformed inner coordinates. The boundary layer on the ramp is seen to have a large wake component relative to the equilibrium turbulent case.

C. Flow separation

Figure 10 shows the distribution of skin friction on the left sidewall ($z/\delta_0 = 0$) and the floor (minimum y coordinate) of the computational domain. The instantaneous skin friction magnitude (magnitude of the mean surface force vector $t_i = \tau_{ji} n_j$) is shown in Fig. 10(a). The dark line near $x/\delta_0 = 2.5$ reflects the presence of the artificial body-force trip. The streaky structure of the shear stress in the spatially developing boundary layer is evident, as are regions where Mach waves from the trip reflect from the sidewalls. Indications of separation are apparent past $x/\delta_0 = 90$ and fingerlike patterns of high shear stress are apparent along the ramp and along the sidewalls. Such patterns may indicate the presence of vortices resulting from an instability associated with

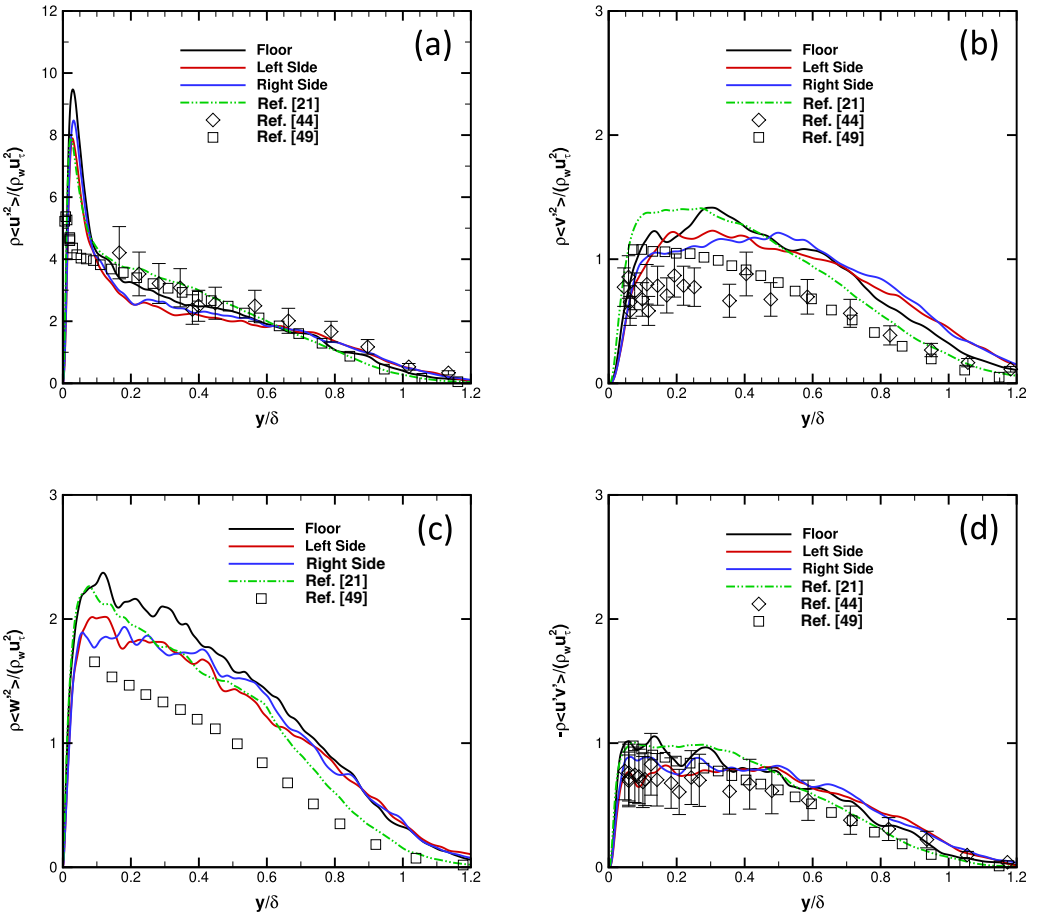

FIG. 8. Profiles of the Reynolds stress on the floor ($x/\delta_0 = 80$ and $z/\delta_0 = 10$) and sides of the domain ($x/\delta_0 = 80$ and $y/\delta_0 = 10$) compared to DNS [21] and to experiment [44,49]: (a) streamwise normal stress $\overline{\rho}\overline{u'^2}$, (b) transverse normal stress $\overline{\rho}\overline{v'^2}$, (c) spanwise normal stress $\overline{\rho}\overline{w'^2}$, and (d) shear stress $-\overline{\rho}\overline{u'v'}$.

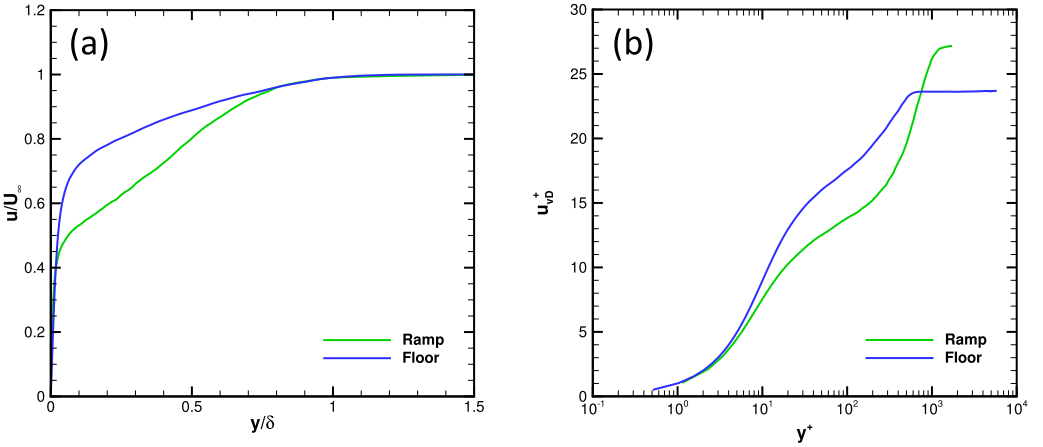

FIG. 9. Turbulent boundary-layer profiles on the floor ($x/\delta_0 = 80$ and $z/\delta_0 = 10$) and on the ramp ($x/\delta_0 \approx 111$ and $z/\delta_0 = 10$): (a) outer coordinates and (b) van Driest transformed inner coordinates.

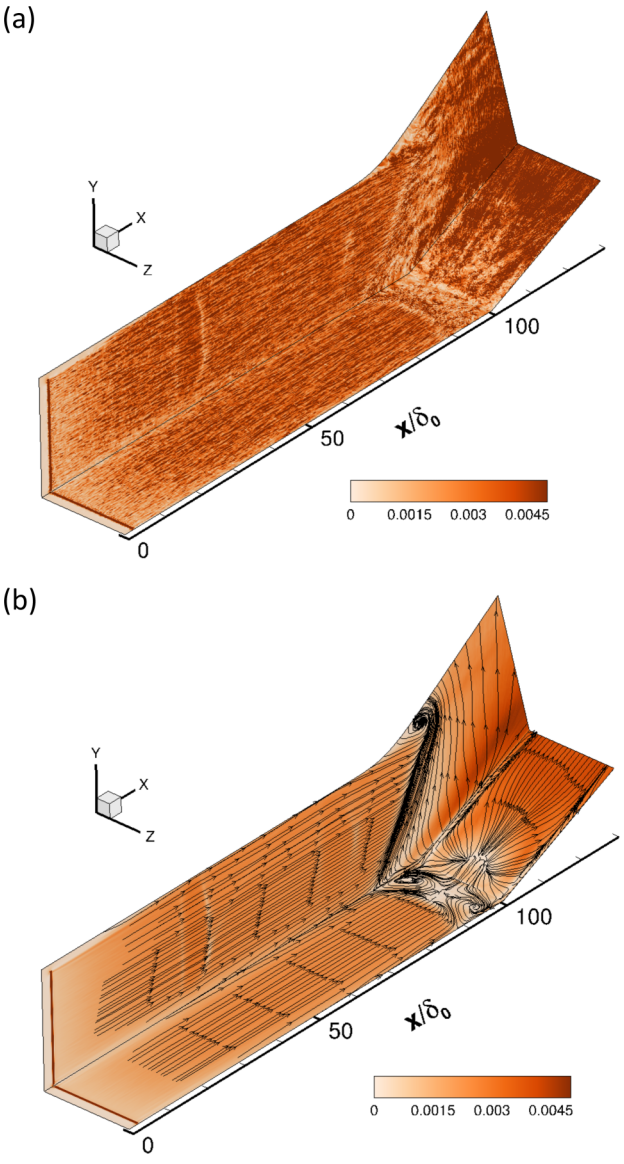

FIG. 10. Skin friction on the left ($z/\delta_0 = 0$) and floor (minimum y coordinate) boundaries of the computational domain: (a) instantaneous values and (b) mean values with trajectories.

streamline curvature [50,51]. In movies of this field of view, indications of Kelvin-Helmholtz-type vortex shedding are also apparent.

The corresponding mean skin friction distribution is presented in Fig. 10(b), with trajectories of the mean surface force vector. Two foci separated by a saddle point are apparent on the bottom wall, with a node on the ramp. There is another focus on the upper sidewall, but this lies near the edge of the resolved region of the computation and thus should be interpreted with caution.

Figure 11 shows a closeup of the distribution of skin friction in the region of separation. In each figure, the view is downstream (x direction); note the axes in Fig. 11(d). The perspective was selected to make the sidewalls visible. The floor of the computational domain is visible at the bottom of the figures, the corner of the ramp is a horizontal line near the bottom third of the field of view,

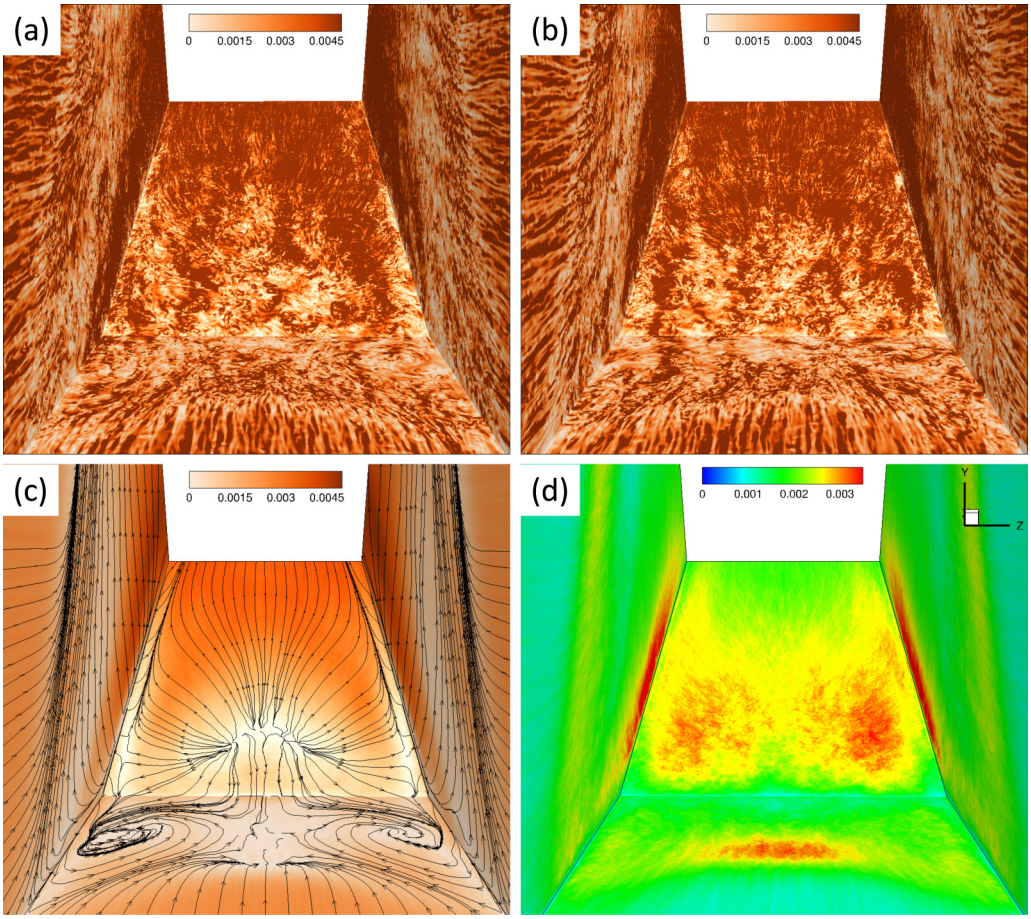

FIG. 11. Skin friction in the region of separation: (a) and (b) examples of instantaneous skin friction, (c) mean skin friction with trajectories, and (d) root-mean-square skin friction.

and the white region at the top of each figure corresponds to the end of the resolved region of the computational domain.

Examples of the instantaneous skin friction magnitude are given in Figs. 11(a) and 11(b). Darker colors indicate higher skin friction, and the beginning of separation is evident as a light band on each wall. Fingerlike regions of high shear stress appear on the ramp; there are typically three to four of these regions. In movies of these data, rotation is evident near the corners where the ramp, floor, and sidewalls intersect. The separation is seen to be asymmetric and highly variable, with large excursions of instantaneous separation and reattachment from their mean locations.

Figure 11(c) shows the magnitude of the mean skin friction. Trajectories of the mean surface force vector are also shown. The flow structure is consistent with a ramp interaction squeezed between two fin interactions. The separation shows a classic owl-face pattern [52], with two stable foci ahead of the ramp separated by a saddle point. A node is present where the mean flow reattaches on the ramp. Stable bifurcation lines are present on both the ramp and the sidewalls.

The root mean square of the skin friction magnitude is shown in Fig. 11(d). Intense fluctuations occur on the centerline of the floor due to intermittent separation there. There are equally intense fluctuations in regions oriented in the streamwise direction on the ramp and on the sidewalls near the corners.

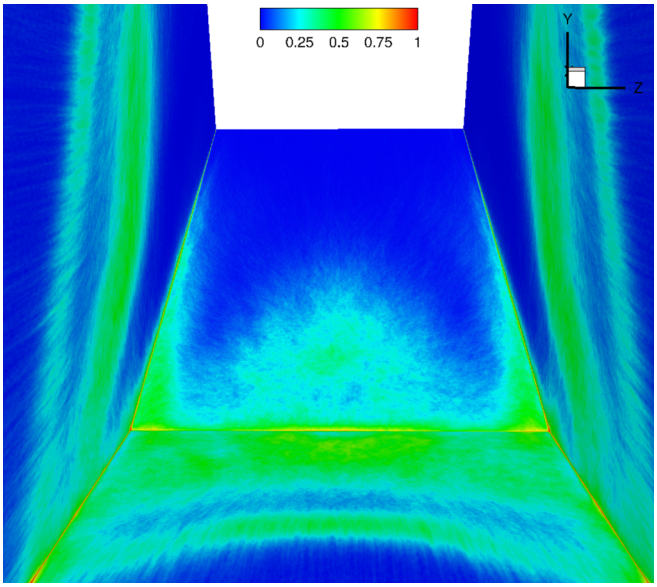

FIG. 12. Probability of low instantaneous skin friction magnitude $P(C_f < 1.0 \times 10^{-3})$.

The unsteady aspects of separation are also addressed in Fig. 12, which shows the probability that the instantaneous skin friction is low, specifically $P(C_f < 1.0 \times 10^{-3})$. The green region corresponds to a probability of 0.5, that is, the region where skin friction is very low about half the time and fairly significant about half the time. This plot highlights the highly intermittent nature of both separation and reattachment and illustrates the large streamwise motions of the separation flow features. It is worth comparing this plot to the mean skin friction in Fig. 11(c) and to the root-mean-square skin friction magnitude shown in Fig. 11(d).

D. Flow confinement effects

In Fig. 13 we compare the present results to an analogous case without sidewall confinement, studied by Porter and Poggie [37]. For that case, the inflow boundary conditions and the flat plate and ramp geometry were the same, but the computation employed a $10\delta_0$ wide configuration with periodic sidewall boundary conditions. Figure 13(a) shows the mean pressure coefficient $C_p = 2(\overline{p} - p_\infty)/\rho_\infty U_\infty^2$ for both cases. For the periodic boundary condition case (labeled "Periodic BC"), the data were averaged across the span. For the case with sidewall confinement (marked "Sidewall Case"), results are shown for the wall centerline ($z/\delta_0 = 10$), that is, the bottom of the field of view shown in Fig. 6 and the bottom centerline of Fig. 10(b). The profile of the floor of the computational domain (minimum y coordinate) is included for orientation. The results for the periodic boundary conditions show the classic mean pressure profile for a two-dimensional shock-wave–boundary-layer interaction: uniform pressure in the incoming boundary layer, a gradual pressure rise to a plateau over the separation region, and a second rise to the pressure level of an inviscid oblique shock corresponding to the ramp turning angle. The present results show somewhat different trends. A slight pressure rise is evident far upstream of the ramp, probably the result of the influence of the corner interactions at the sidewalls. The separated region is smaller. Farther downstream, the pressure reaches a maximum, rather than smoothly approaching the inviscid pressure rise. This behavior is a result of the three-dimensional shock interaction, as seen, for example, in Fig. 5.

The corresponding profiles of the streamwise skin friction coefficient are shown in Fig. 13(b). For both flows, there is a rapid drop in skin friction at separation, a pattern with two minima within the

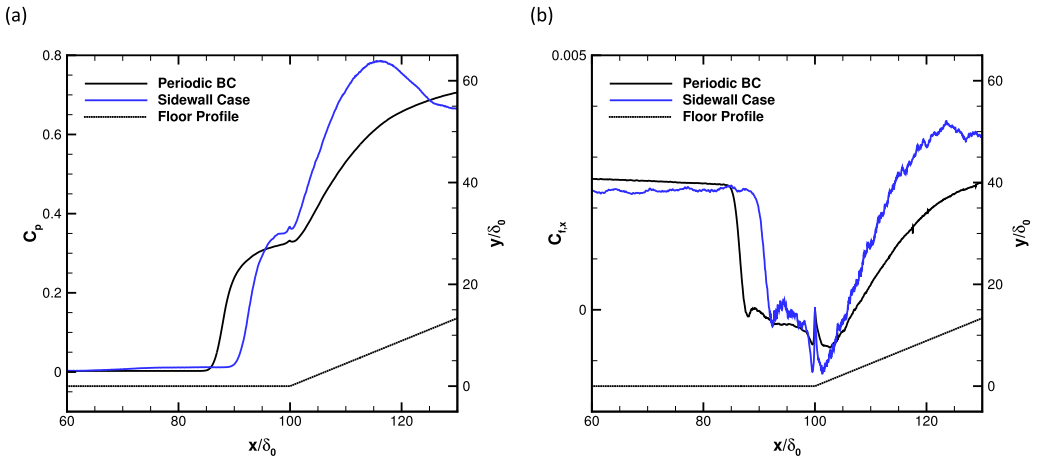

FIG. 13. Profiles along the centerline of the interaction compared to the analogous case with periodic sidewall boundary conditions [37]: (a) mean pressure coefficient and (b) mean streamwise skin friction coefficient.

separation zone, and a gradual increase downstream as the reattached boundary layer recovers. (The spike at $x/\delta_0 = 100$ is a numerical artifact due to the presence of the corner.) The double minimum in the skin friction within the separated zone has been observed in previous studies of compression ramp interactions [36,53]. [See also the mean flow structure in Figs. 10(b) and 11(c).] Again, note the decreased streamwise extent of separation that occurs with the presence of the sidewalls.

Table III presents the streamwise length scale L_s/δ of the mean separation on the centerline of the interaction as a function of the aspect ratio δ/w. The present results are given along with results from our previous spanwise-periodic calculations [37] and the data of Bisek [19]. We note that the conditions of Bisek's calculations are not quite the same as our own: The initial flat plate was $85\,\delta_0$ long in his work and $100\,\delta_0$ long in our own work. The trend is suggestive in Table III, but it would require additional calculations to determine whether the curvilinear relationship of separation length and aspect ratio predicted by Babinsky *et al.* [12] for reflected shock interactions also occurs for compression ramp flows.

E. Symmetry and antisymmetry

Figure 14 shows the wall pressure distribution in the region of separation. The mean pressure is shown in Fig. 14(a) and the root-mean-square pressure fluctuation is shown in Fig. 14(b). The corner flow interaction is seen to lead to strong variation in the mean pressure along the spanwise (z) direction. Intense pressure fluctuations are observed far upstream of the ramp, particularly in the corner regions. Severe fluctuations are also present in fingerlike regions on the ramp and near the juncture of the ramp and sidewalls.

TABLE III. Centerline separation length scale as a function of interaction confinement for Mach 2.25 flow over a 24° ramp.

δ/w	L_s/δ	Reference
0.00	8.4	[37]
0.06	7.2	[19]
0.12	6.0	present work

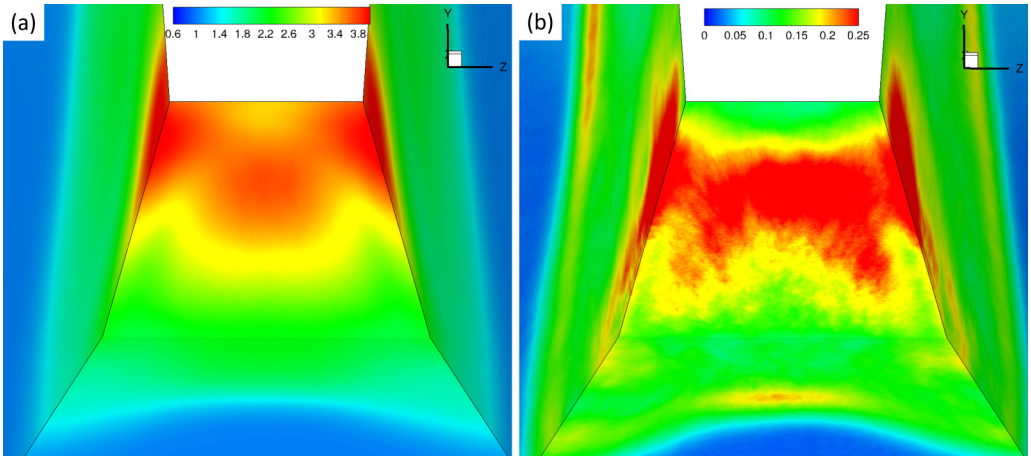

FIG. 14. Wall pressure in the region of separation: (a) mean pressure $\overline{p}/p_\infty$ and (b) root-mean-square pressure fluctuation intensity $(\overline{p'^2})^{1/2}$.

Although the mean flow field is symmetric, the instantaneous flow field can be highly asymmetric, as seen in Figs. 11(a) and 11(b). Given that symmetry plane boundary conditions are often employed in large-eddy simulations for savings in computational cost, it is of interest to examine symmetric and antisymmetric motions in the present full-span computation. A qualitative exploration of these effects was presented by Bisek [19]. Here we quantify the analysis of large-scale symmetric and antisymmetric motions of the separation zone using conditional averaging.

Figure 15 shows the regions selected to determine the condition variable for the conditional averages. Two regions of equal area on the floor of the domain (minimum y coordinate) were selected. In each case, the spatial averages of the pressure over region A and region B were computed for a given instant in time. Condition 1 [Fig. 15(a)] was true if $\overline{p}_A - \overline{p}_B > 0.14\,\overline{p}_{AB}$ and was selected to capture events with high pressure at the edges of the domain, that is, sidewall separation farther upstream. Condition 2 [Fig. 15(b)] was true if $\overline{p}_A - \overline{p}_B > 0.01\,\overline{p}_{AB}$ and was selected to capture large-scale asymmetric motions of the separation region.

Figure 16 shows the results for condition 1. The contours show the deviation of the conditional average from the overall average [see Fig. 14(a)]. This condition was true for 32.8% of the samples: There was high pressure at the edges about one-third of the time. The results for condition 1 are shown in Fig. 16(a) and complementary average (condition not true) is shown in Fig. 16(b). Although the condition variable is based on the pressure on the floor of the domain (minimum y coordinate), significant changes are seen elsewhere in the domain. High pressures exist on the sidewalls when pressures are high on the floor of the domain and vice versa. This is consistent with a forward-backward motion of the separation shock system.

Figure 17 shows the results obtained for condition 2. Again, the contours show the deviation of the conditional average from the overall average. The results for condition 2 are shown in Fig. 17(a) and the complementary average (condition not true) is shown in Fig. 17(b). Condition 2 was true for 40.5% of the samples: There was high pressure on the right side almost half the time. The results for these conditional averages seem to be consistent with an antisymmetric left-right motion of the shock system. When pressures increase on one side of the domain, they decrease on the other side.

The conditional averages have highlighted large-scale symmetric and antisymmetric modes of the separation zone. The results do not stem from spurious correlation: They identify frequent events, and consistent flow changes are observed away from the condition region.

To further explore the issue of the symmetry of the instantaneous flow, a correlation analysis of the wall pressure was carried out and the results were compared to analogous data for the periodic

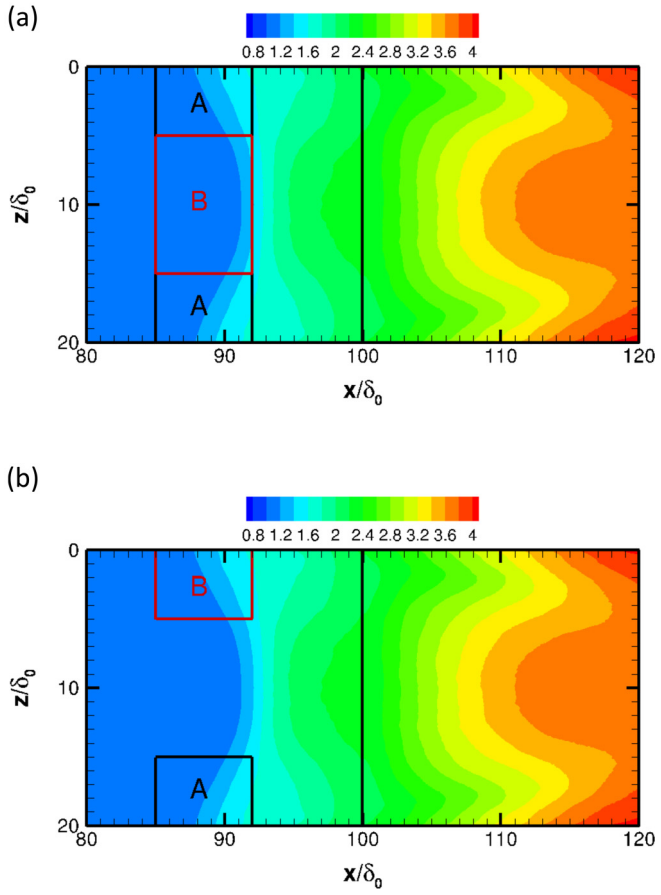

FIG. 15. Mean pressure contours $\overline{p}/p_\infty$ on floor of computational domain, along with regions used for conditional averages: (a) condition 1, looking for high pressures at the edges, and (b) condition 2, looking for high pressure on the right side.

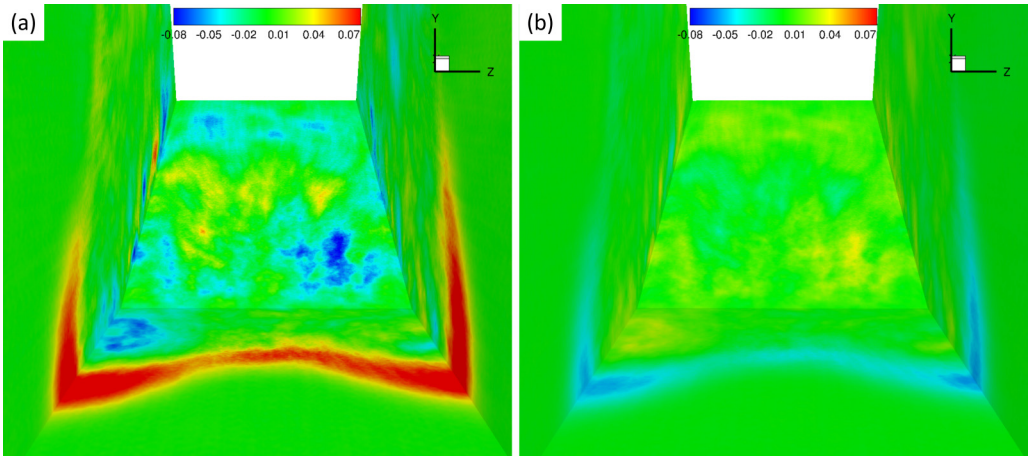

FIG. 16. Deviation from overall mean for conditional averages of the pressure field: (a) high pressures at the edges (32.8% of samples) and (b) complementary average (67.2% of samples).

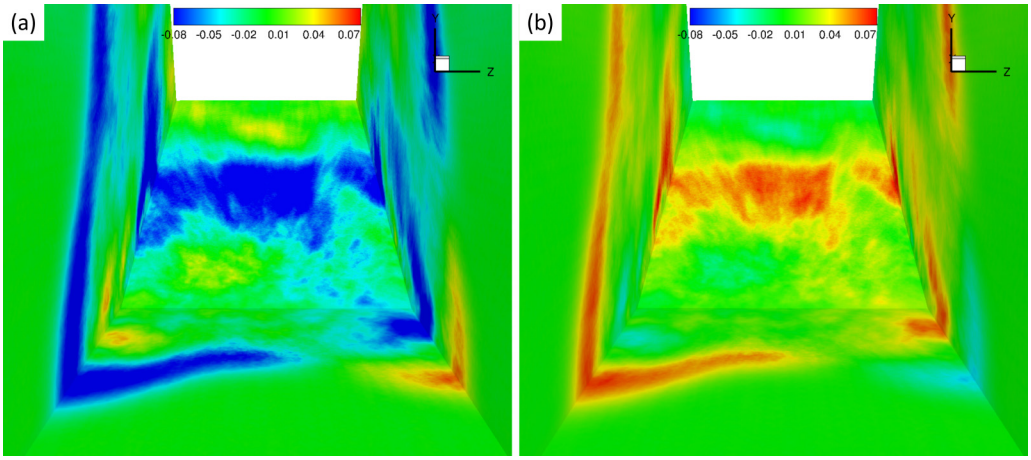

FIG. 17. Deviation from overall mean for conditional averages of the pressure field: (a) high pressures on the right side (40.5% of samples) and (b) complementary average (59.5% of samples).

open sidewall case [37]. Specifically, two-point spatial correlations $R(x, y, z, x_r, y_r, z_r)$ of the wall pressure signal were carried out for zero time delay and for a fixed reference point (x_r, y_r, z_r).

Figure 18 shows the correlations for the present flow, which is confined by sidewalls, and Fig. 19 shows corresponding correlations for the periodic sidewall case. (See Fig. 13 for orientation relative to separation and reattachment.) For Fig. 18(a), the reference point is located on the centerline, just upstream of mean flow separation ($x_r/\delta_0 = 91.0$ and $z_r/\delta_0 = 10.0$). Comparing to the analogous case for the periodic flow [Fig. 19(a), $x_r/\delta_0 = 86.9$ and $z_r/\delta_0 = 5.0$], a remarkable correlation along the mean separation line all the way around the duct sidewalls is observed. A significant correlation ($R \geqslant 0.5$) between separation and reattachment is observed in the sidewall case and is not present in the periodic boundary condition case. When the reference point for the correlation is shifted to a station near the sidewall [Fig. 18(b), $x_r/\delta_0 = 91.0$ and $z_r/\delta_0 = 0.1$], similar results are obtained, except that the correlation appears to be responding primarily to an asymmetric motion of the separation zone.

Corresponding results for a reference point just downstream of reattachment are shown in Fig. 18(c) for the sidewall case (reference point: $x_r/\delta_0 = 106.0$ and $z_r/\delta_0 = 10.0$) and Fig. 19(b) for the periodic case (reference point: $x_r/\delta_0 = 108.7$ and $z_r/\delta_0 = 5.0$). Here the correlations appear to be responding to localized events near reattachment. For a reference point at an analogous station in the corner flow region [Fig. 18(c), $x_r/\delta_0 = 106.0$ and $z_r/\delta_0 = 0.1$], interaction between the ramp and sidewall flows is apparent, as is an asymmetry along the spanwise (z) direction.

IV. CONCLUSION

Numerical simulations were carried out to examine the effect of sidewalls on a Mach 2.25, 24° compression ramp interaction in which the confinement effect was very strong ($\delta/w = 0.12$). Inflow conditions were chosen to match previous simulations and thus explore the effect of the domain width parameter on the flow structure.

The inflow boundary condition was specified as a laminar-flow similarity solution for the selected flow conditions. Interpolation was used to produce smooth flow in the corners of the domain. Transition to turbulent flow was promoted using an artificial body-force trip. The computed incoming flow at the $x/\delta_0 = 80$ station was compared to the results of direct numerical simulations and experiments and judged to be a well-developed turbulent boundary layer along the three walls, with $M_\infty = 2.25$, $\mathrm{Re}_{\theta i} = 1800$, and $\delta^+ = 540$.

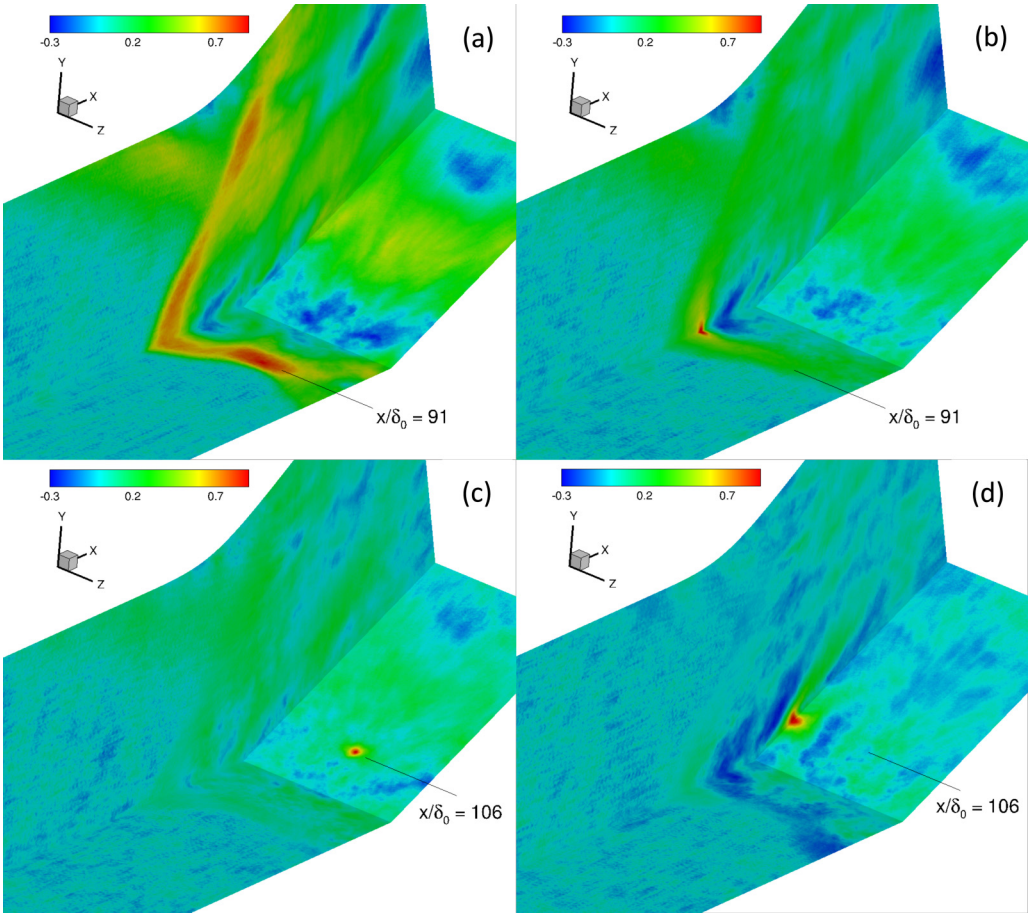

FIG. 18. Spatial correlation of wall pressure: (a) reference point $x_r/\delta_0 = 91.0$, $z_r/\delta_0 = 10.0$, (b) reference point $x_r/\delta_0 = 91.0$, $z_r/\delta_0 = 0.1$, (c) reference point $x_r/\delta_0 = 106.0$, $z_r/\delta_0 = 10.0$, and (d) reference point $x_r/\delta_0 = 106.0$, $z_r/\delta_0 = 0.1$.

The ratio of turbulent boundary-layer thickness to domain width at the start of the interaction was $\delta/w = 0.12$, close to the limit of flow choking, and the overall flow structure was found to be complex. A region near the centerline of the domain resembled a two-dimensional compression ramp flow in structure. Nonetheless, this region was very narrow, confined by sidewall flows that resembled fin interactions.

The instantaneous flow was found to be intensely unsteady, to an extent that is difficult to convey in still images. (Animations of several of the views shown in the figures from this article are available in [54].) Separation and reattachment moved significantly in the streamwise direction and reattachment was characterized by unsteady streamwise structures along the ramp. Very intense fluctuations in pressure and skin friction occurred in the corners along the ramp, with additional maxima near centerline separation and reattachment.

Significant differences in flow structure were observed between computations with confining sidewalls and computations with periodic or symmetric boundary conditions at the lateral boundaries of the domain. Comparing to the limited data available from similar computations, the centerline separation length scale L_s/δ was seen to vary with the flow confinement parameter δ/w, as previously recognized in reflected shock interactions. Investigation of the instantaneous flow structure identified large-scale symmetric and antisymmetric motions.

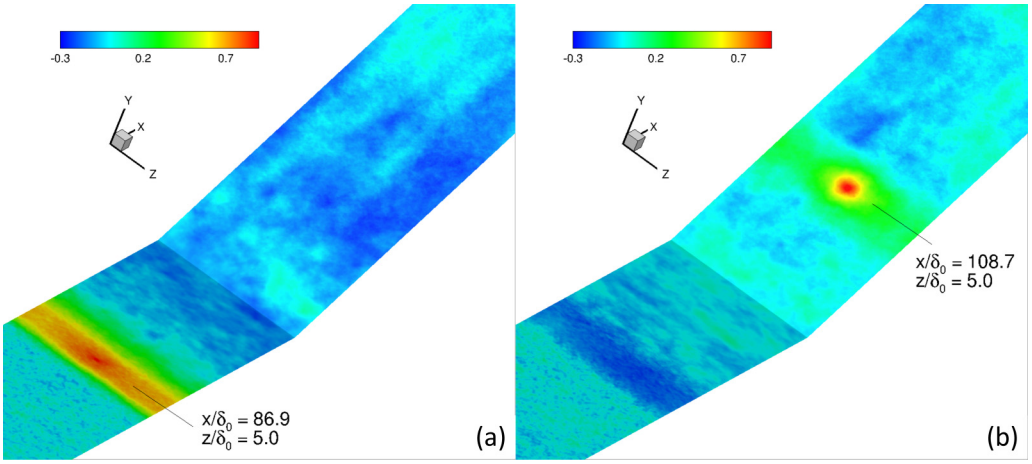

FIG. 19. Spatial correlation of wall pressure for the case with periodic sidewall boundary conditions [37]: (a) reference point $x_r/\delta_0 = 86.9$, $z_r/\delta_0 = 5.0$ and (b) reference point $x_r/\delta_0 = 108.7$, $z_r/\delta_0 = 5.0$.

The influence of sidewalls on shock-wave–boundary-layer interactions is seen to be significant, and this effect is worthy of additional research attention. Subsonic corner flows offer a path for upstream propagation of disturbances that is expected to influence unsteadiness in many practical situations.

ACKNOWLEDGMENTS

Support for this work was provided by Purdue University, by AFOSR Grant No. FA9550-17-1-0153 monitored by I. Leyva, and by an award of computer time provided by the DOE INCITE program. This research used resources of the Argonne Leadership Computing Facility, which is a DOE Office of Science User Facility supported under Contract No. DE-AC02-06CH11357. Some additional calculations and postprocessing were carried out at the Air Force Research Laboratory DOD Supercomputing Resource Center.

[1] S. Bogdonoff, Some experimental studies of the separation of supersonic turbulent boundary layers, Princeton University, Department of Aeronautical Engineering Report No. 336, 1955 (unpublished).
[2] A. L. Kistler, Fluctuating wall pressure under a separated supersonic flow, J. Acoust. Soc. Am. **36**, 543 (1964).
[3] J. E. Green, Interactions between shock waves and turbulent boundary layers, Prog. Aerosp. Sci. **11**, 235 (1970).
[4] D. S. Dolling, Fifty years of shock-wave/boundary-layer interaction research: What next? AIAA J. **39**, 1517 (2001).
[5] J.-P. Dussauge and S. Piponniau, Shock/boundary-layer interactions: Possible sources of unsteadiness, J. Fluids Struct. **24**, 1166 (2008).
[6] J. R. Edwards, Numerical simulations of shock/boundary layer interactions using time-dependent modeling techniques: A survey of recent results, Prog. Aerosp. Sci. **44**, 447 (2008).
[7] N. T. Clemens and V. Narayanaswamy, Low-frequency unsteadiness of shock wave/turbulent boundary layer interactions, Annu. Rev. Fluid Mech. **46**, 469 (2014).
[8] D. V. Gaitonde, Progress in shock wave/boundary layer interactions, Prog. Aerosp. Sci. **72**, 80 (2015).

[9] D. C. Reda and J. D. Murphy, Shock wave/turbulent boundary-layer interactions in rectangular channels, AIAA J. **11**, 139 (1973).
[10] D. C. Reda and J. D. Murphy, Sidewall boundary-layer influence on shock wave/turbulent boundary-layer interactions, AIAA J. **11**, 1367 (1973).
[11] D. M. F. Burton and H. Babinsky, Corner separation effects for normal shock wave/turbulent boundary layer interactions in rectangular channels, J. Fluid Mech. **707**, 287 (2012).
[12] H. Babinsky, J. Oorebeek, and T. G. Cottingham, *Proceedings of the 51st AIAA Aerospace Sciences Meeting Including the New Horizons Forum and Aerospace Exposition* (American Institute of Aeronautics and Astronautics, Reston, 2013), paper 2013-0859.
[13] J. A. Benek, C. J. Suchyta, and H. Babinsky, *Proceedings of the 51st AIAA Aerospace Sciences Meeting Including the New Horizons Forum and Aerospace Exposition* (Ref. [12]), paper 2013-0862.
[14] M. Pizzella, S. Warning, M. McQuilling, A. Purkey, R. Scharnhorst, M. Mani, J. Benek, C. J. Suchyta, and H. Babinsky, *Proceedings of the 55th AIAA Aerospace Sciences Meeting* (American Institute of Aeronautics and Astronautics, Reston, 2017), paper 2017-0535.
[15] E. Garnier, Stimulated detached eddy simulation of three-dimensional shock/boundary layer interaction, Shock Waves **19**, 479 (2009).
[16] M. Funderburk and V. Narayanaswamy, Experimental investigation of primary and corner shock boundary layer interactions at mild back pressure ratios, Phys. Fluids **28**, 086102 (2016).
[17] B. Morgan, K. Duraisamy, and S. K. Lele, Large-eddy simulations of a normal shock train in a constant-area isolator, AIAA J. **52**, 539 (2014).
[18] B. Wang, N. D. Sandham, Z. Hu, and W. Liu, Numerical study of oblique shock-wave/boundary-layer interaction considering sidewall effects, J. Fluid Mech. **767**, 526 (2015).
[19] N. J. Bisek, *Proceedings of the 53rd AIAA Aerospace Sciences Meeting* (American Institute of Aeronautics and Astronautics, Reston, 2015), paper 2015-1976.
[20] F. M. White, *Viscous Fluid Flow*, 2nd ed. (McGraw-Hill, New York, 1991).
[21] J. Poggie, N. J. Bisek, and R. Gosse, Resolution effects in compressible, turbulent boundary layer simulations, Comput. Fluids **120**, 57 (2015).
[22] S. K. Lele, Compact finite difference schemes with spectral-like resolution, J. Comput. Phys. **103**, 16 (1992).
[23] D. V. Gaitonde and M. R. Visbal, High-order schemes for Navier-Stokes equations: Algorithm implementation into FDL3DI, Wright-Patterson Air Force Base, Air Force Research Laboratory Report No. AFRL-VA-WP-TR-1998-3060, 1998, https://apps.dtic.mil/dtic/tr/fulltext/u2/a364301.pdf.
[24] M. R. Visbal and D. V. Gaitonde, On the use of higher-order finite-difference schemes on curvilinear and deforming meshes, J. Comput. Phys. **181**, 155 (2002).
[25] M. R. Visbal and D. V. Gaitonde, *Proceedings of the 43rd Aerospace Sciences Meeting and Exhibit* (American Institute of Aeronautics and Astronautics, Reston, 2005), paper 2005-1265.
[26] R. C. Swanson and E. Turkel, On central-difference and upwind schemes, J. Comput. Phys. **101**, 292 (1992).
[27] J. Morrison, *Proceedings of the 2nd International Aerospace Planes Conference* (American Institute of Aeronautics and Astronautics, Reston, 1990), paper 90-5251.
[28] W. K. Anderson, J. L. Thomas, and B. van Leer, Comparison of finite volume flux vector splittings for the Euler equations, AIAA J. **24**, 1453 (1986).
[29] M. R. Visbal and D. P. Rizzetta, Large-eddy simulation on curvilinear grids using compact differencing and filtering schemes, J. Fluid. Eng. **124**, 836 (2002).
[30] T. H. Pulliam and D. S. Chaussee, A diagonal form of an implicit approximate-factorization algorithm, J. Comput. Phys. **39**, 347 (1981).
[31] T. H. Pulliam and J. L. Steger, Implicit finite-difference simulations of three-dimensional compressible flow, AIAA J. **18**, 159 (1980).
[32] P. D. Thomas and C. K. Lombard, Geometric conservation law and its application to flow computations on moving grids, AIAA J. **17**, 1030 (1979).
[33] M. M. Rai, T. B. Gatski, and G. Erlebacher, *Proceedings of the 33rd Aerospace Sciences Meeting and Exhibit* (American Institute of Aeronautics and Astronautics, Reston, VA, 1995), paper 95-583.

[34] S. Pirozzoli, F. Grasso, and T. B. Gatski, Direct numerical simulation and analysis of a spatially evolving supersonic turbulent boundary layer at $M = 2.25$, Phys. Fluids **16**, 530 (2004).
[35] D. P. Rizzetta and M. R. Visbal, Large-eddy simulation of supersonic boundary-layer flow by a high-order method, Int. J. Comput. Fluid Dyn. **18**, 15 (2004).
[36] N. Bisek, D. Rizzetta, and J. Poggie, Plasma control of a turbulent shock boundary-layer interaction, AIAA J. **51**, 1789 (2013).
[37] K. M. Porter and J. Poggie, Selective upstream influence on the unsteadiness of a separated turbulent compression ramp flow, Phys. Fluids **31**, 016104 (2019).
[38] N. J. Georgiadis, D. P. Rizzetta, and C. Fureby, Large-eddy simulations: Current capabilities, recommended practices, and future research, AIAA J. **48**, 1772 (2010).
[39] N. J. Mullenix, D. V. Gaitonde, and M. R. Visbal, Spatially developing supersonic turbulent boundary layer with a body-force-based method, AIAA J. **51**, 1805 (2013).
[40] J. C. Gonsalez and D. S. Dolling, *Proceedings of the 31st Aerospace Sciences Meeting* (American Institute of Aeronautics and Astronautics, Reston, 1993), paper 93-0776.
[41] P. Dupont, C. Haddad, and J. F. Debieève, Space and time organization in a shock-induced separated boundary layer, J. Fluid Mech. **559**, 255 (2006).
[42] J. W. Nichols, J. Larsson, M. Bernardini, and S. Pirozzoli, Stability and modal analysis of shock/boundary layer interactions, Theor. Comput. Fluid Dyn. **31**, 33 (2017).
[43] J. Poggie, P. J. Erbland, A. J. Smits, and R. B. Miles, Quantitative visualization of compressible turbulent shear flows using condensate-enhanced Rayleigh scattering, Exp. Fluids **37**, 438 (2004).
[44] M. Éléna and J. P. Lacharme, Experimental study of a supersonic turbulent boundary layer using a laser Doppler anemometer, J. Mec. Theor. Appl. **7**, 175 (1988).
[45] S. Piponniau, J. P. Dussauge, J. F. Debiève, and P. Dupont, A simple model for low-frequency unsteadiness in shock-induced separation, J. Fluid Mech. **629**, 87 (2009).
[46] S. Pirozzoli and M. Bernardini, Turbulence in supersonic boundary layers at moderate Reynolds number, J. Fluid Mech. **688**, 120 (2011).
[47] E. R. van Driest, On the turbulent flow near a wall, J. Aeronaut. Sci. **23**, 1007 (1956).
[48] M. V. Morkovin, in *Méchanique de la Turbulence*, edited by A. Favre (CNRS, Paris, 1962), pp. 367–380.
[49] A. E. Alving, Boundary layer relaxation from convex curvature, Ph.D. thesis, Princeton University, 1988.
[50] S. Navarro-Martinez and O. R. Tutty, Numerical simulation of Görtler vortices in hypersonic compression ramps, Comput. Fluids **34**, 225 (2005).
[51] S. Priebe, J. H. Tu, C. W. Rowley, and M. P. Martín, Low-frequency dynamics in a shock-induced separated flow, J. Fluid Mech. **807**, 441 (2016).
[52] A. E. Perry and M. S. Chong, A description of eddying motions and flow patterns using critical point concepts, Annu. Rev. Fluid Mech. **19**, 125 (1987).
[53] S. Priebe and M. P. Martín, Low-frequency unsteadiness in shock wave-turbulent boundary layer interaction, J. Fluid Mech. **699**, 1 (2012).
[54] https://engineering.purdue.edu/~jpoggie/sidewalls/.